Editors' Choice—How the Infinitesimally Small K+-Crossover Enables Sufficient Ionic Coupling in Ionomer-Free Thin-Form Factor Nanoelectrodes for Catholyte-Free Water Electrolysis

To cite this article: Venkataramana Rishikesan *et al* 2026 *ECS Adv.* **5** 024501

ECS Advances, 2026 **5** 024501

Editors' Choice—How the Infinitesimally Small K+-Crossover Enables Sufficient Ionic Coupling in Ionomer-Free Thin-Form Factor Nanoelectrodes for Catholyte-Free Water Electrolysis

Venkataramana Rishikesan,[1,2,3] Martijn J. W. Blom,[1,3] Patrick Steegstra,[1,3] Rico Rupp,[1,3] and Philippe M. Vereecken[1,2,3,*,z]

[1] *imec, Leuven, 3001, Belgium*
[2] *KU-Leuven, M²S, Centre for Membrane Separations, Adsorption, Catalysis, and Spectroscopy for Sustainable Solutions, Leuven, 3001, Belgium*
[3] *EnergyVille, Genk, 3600, Belgium*

Conventional anion exchange membrane (AEM) water electrolyzers are largely dependent on ionomeric binders. While ionomers provide ionic coupling and maintain the structural integrity of electrodes, they are also known to block catalytic active sites and chemically degrade with time. In this work, we present a way to operate our Ni nanomesh integrated AEM water electrolyzer with no added ionomers and without an electrolyte supply to the cathode, i.e., catholyte-free. A nanomesh is an integrated electrode comprising of billions of nanowires, horizontally and vertically crosslinked, mechanically stabilized on an open support structure. Moreover, the catholyte-free operation relies on the thin form factor of the nanomesh electrodes (4 μm) and the cross-over of potassium ions to the nanomesh cathode and supplied from the anolyte through the membrane. The thinness of the nanomesh electrodes combined with the intrinsic property of a membrane to allow tiny amounts of water to pass through it enabled the catholyte-free operation. Furthermore, for the first time, the unintended cross-over of potassium ions (K^+) across an AEM is taken advantage of, to build an operando KOH environment on demand, facilitating ionic coupling in the absence of ionomers hence providing valuable insights for the optimization of AEM water electrolyzer systems.
 [DOI: 10.1149/2754-2734/ae5bc9]

Manuscript submitted November 24, 2025; revised manuscript received March 31, 2026. Published April 27, 2026.

Supplementary material for this article is available online

Anion (OH^--ion) exchange membrane (AEM) waterelectrolyzer technology has the potential to combine the best features of the more mature alkaline water electrolyzer (AWE) and proton exchange membrane (PEM) water electrolyzer technology, making it an attractive option for the future of green H_2 industry.[1–4] AEM water electrolyzers enable the use of inexpensive Ni-based electrodes combined with the flexibility to be coupled with the intermittent nature of renewable energy sources (RES).[5,6] Moreover, they are relatively compact in size and can operate at higher current densities compared to an AWE (hundreds of mA cm^{-2} vs thousands of mA cm^{-2}).[7,8] In our previous work, we presented a methodology to fabricate high surface area 3D interconnected Ni nanomesh electrodes and compared it to commercially available Ni foam electrodes in an AEM electrolyzer setup. The nanomesh electrode, with a thickness of just 4 μm, demonstrated a significantly better performance compared to commercially available Ni foam electrodes, which are 1600 μm thick, when a 1 M KOH solution was supplied at both the anode and cathode. In effect, the thinner nanomesh electrodes concentrate all the electrochemically active sites 2-orders of magnitude closer to the membrane whilst maintaining a 110x surface area enhancement (110 cm^2 per geometric cm^2).

The whole Ni nanomesh electrode is an integrated electrode that is comprised of a highly porous few-micrometers-thin nanomesh that is mechanically supported by and suspended over an open Ni support structure as shown in Fig. 1c (SEM images presented in Fig. S1). The nanomesh is known to offer around 30x surface area enhancement per micron thickness while maintaining a porosity around 76%, resulting in a densely arranged, billions of inter-connected horizontal and vertical nanowires (40 nm in diameter and 64 nm apart).[9–11] For a 4-micrometer thin nanomesh used in this work, the nanomesh geometry has an internal surface area of around 110x. In this work, we extended the operating scope of our Ni nanomesh integrated AEM water electrolyzer by eliminating electrolyte supply to the cathode, i.e., catholyte-free as shown in Fig. 1a. The catholyte-free electrolyzer of this work was configured by simply placing the Ni nanomesh electrodes on both the sides of a commercial AEM which operated in a low concentration (1 M KOH) electrolyte solution that is fed only to the anode. Apart from the freedom to rationally design the nanomesh geometry for optimum mass transport, a catholyte-free electrolyzer introduces a facile approach to operating an electrolyzer that can lead to simplification of plant-scale operation, i.e., eliminating the need for manifold, piping related to all cathodes in a stack and the cathode gas-liquid separator. Moreover, eliminating the catholyte in electrolyzer stacks removes the medium in the manifolds through which undesired leakage of ionic currents take place leading to crosstalk between cells in a stack.[12–15] Additional benefits of going catholyte-free include reduced resistance to H_2 gas flow (inside the electrode and perpendicular to the membrane) due to the absence of an electrolyte-flow in the opposite direction and reduced bubble coverage of the cathode. Finally, the catholyte-free electrolyzer of this work resembles the operation of a gas diffusion electrode based electrochemical device and will indeed form the foundation for enabling electrolysis of sparingly soluble gases such as CO_2 and N_2 using the nanomesh electrodes.

In fact, state-of-the-art AEM water electrolyzers already operate in a catholyte-free manner with low concentration KOH (0.1–1 M) fed to the anode. This is partially achieved using polymeric anion conductive binders known as ionomers within the porous electrodes. These ionomers typically contain a large concentration of mobile hydroxide ions (OH^-) which provides the ionic coupling between the distant electroactive sites on the electrode and the membrane. While the low concentration KOH at the anode is sufficiently conductive, especially considering that the electrodes are only few tens of microns thick, the ionomeric network in electrolyte-free cathode plays an important role in ionically coupling the porous cathode. Traditionally, such electrodes are fabricated by applying catalytic ink (few tens of microns thick) on both sides of a conductive membrane that allows the selective movement of anions across it (ideally OH^-), thus forming the so-called catalyst coated

*Electrochemical Society Member.
zE-mail: philippe.vereecken@imec.be

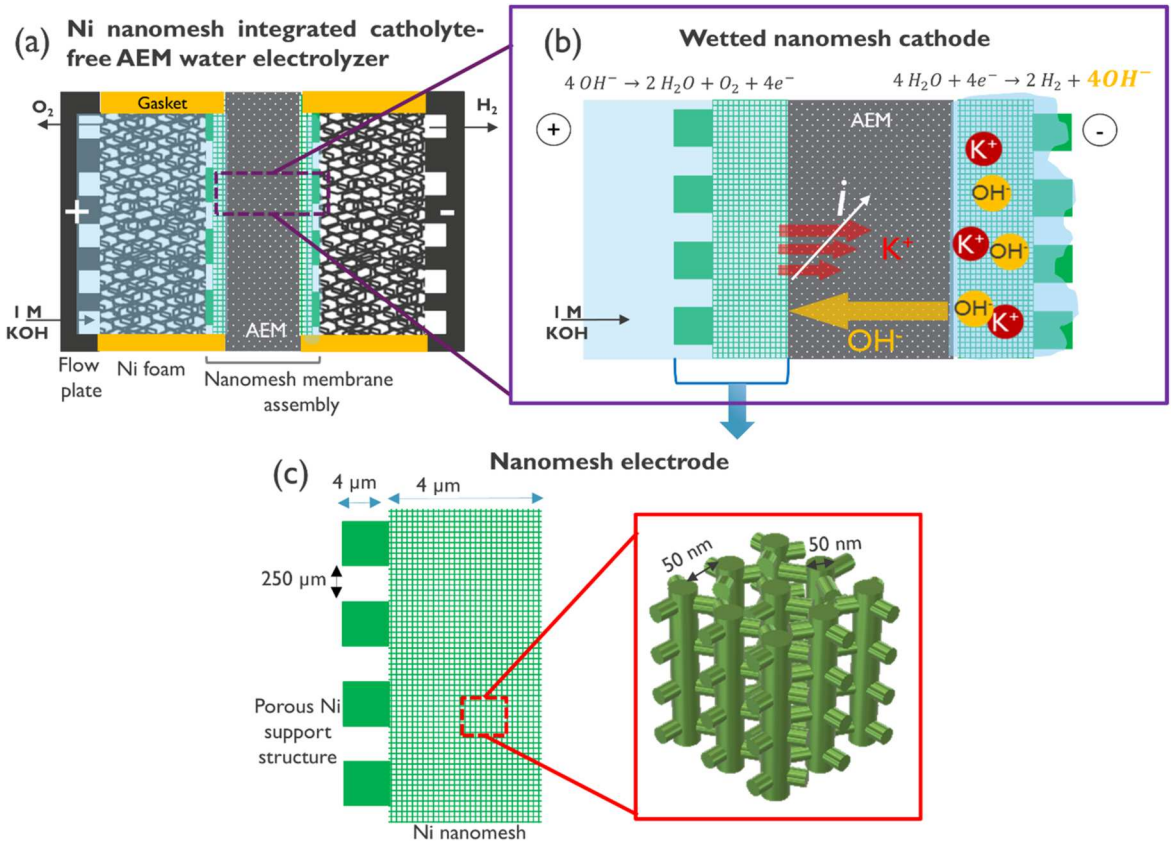

Figure 1. (a) Schematic of a Ni nanomesh (4 μm nanomesh + 4 μm support structure) integrated AEM water electrolyzer operating in a catholyte-free mode. Catholyte-free electrolyzer is operated by passing 1 M KOH over the Ni nanomesh anode at a flow rate of 49 ml min^{-1} and no electrolyte supply to the Ni nanomesh cathode. Commercial 1.6 mm thick Ni foams were used to back contact the nanomesh electrodes. (b) Schematic of the nanomesh membrane assembly of the catholyte-free electrolyzer depicting a wetted nanomesh cathode under operation. The migration driven flux of K^+ is shown to be current density dependent. (c) 2D- cross-sectional schematic of a Ni nanomesh electrode comprised of a 4 μm Ni nanomesh that is mechanically supported on a 4 μm open Ni support structure. The open Ni support structure has 250 μm sized openings to facilitate mass-transfer in and out of the nanomesh electrode. The zoomed in 3D-schematic represents the structure of the nanomesh showcasing the inter-connected vertical and horizontal nanowires. Note that cross sectional schematic is drawn out of scale to show all features of the nanomesh electrode.

membrane (CCM). The catalytic ink that makes up the porous electrodes is composed of carbon particles for electronic conduction, catalyst nanoparticles promoting hydrogen and oxygen evolution reactions, and ionomers.[16,17] In addition to the OH^- conduction provided by ionomers, it also functions as a glue to bind all the particulate components together eventually forming the electrode. It is worth mentioning that in our approach we avoid the use of any added ionomers. This is possible because the nanomesh electrodes are monolithic and structurally stable by themself. This means there is no need for a binder to maintain the mechanical stability of the nanomesh electrode. Furthermore, ionic coupling within our nanomesh cathodes in the absence of ionomers is provided by an in operando KOH electrolyte environment as will be demonstrated below. In this case, in operando means the formation of a KOH like environment inside the nanomesh cathode during electrolyzer operation. Note that there are various ionomer-free electrodes that have already been reported for AEM water electrolyzers.[18–20] In most cases, the electrodes are prepared by sputtering metals such as Ni and Fe on porous transport layers like carbon paper and porous foams. In fact, in our previous work, we showed that large surface area Pt nanomesh electrodes were able to produce H_2 at 1 A cm^{-2}_{geo} from DI water even in the absence of ionomers.[21] Such a process was facilitated by the confinement of the electrogenerated species such as H^+ and OH^- within the 50 nm wide nanochannels that made up the Pt nanomesh. While there was an additional 450-mV overpotential required to operate at higher current densities in DI water as compared to operating in 1 M H_2SO_4, utilizing the cation-crossover effect can eliminate this penalty, as discussed in detail in this work. While these electrodes are reported to display decent performance, the nanomesh electrode of this work can offer several advantages including a controllable structure for optimum mass transport, a high surface area concentrated in a few microns thickness and a monolithic structure alleviating the dangers of catalyst particle detachment - especially for binder-free electrodes. However, this work does not focus on the comparison of performance metrics with state of the art.

We further demonstrate that the catholyte-free operation was enabled by the thinness (4 μm) of the nanomesh electrode combined with the intrinsic property of the membrane to allow tiny amounts of water to pass through it, hence forming a layer of liquid. Interestingly, this liquid layer was sufficient to wet the nanomesh electrode, thereby preserving its electrochemical active surface area (see Fig. 1b). Commercially available Ni foam electrodes were too thick and have too large pore sizes to utilize these effects. A water-only wetted nanomesh cathode would introduce a large electrolyte resistance, especially considering the thickness of the nanomesh electrode of around 4 μm. However, our data suggests complete utilization of the nanomesh electrode thickness, i.e. the full 4 micrometers.

The fact that no additional overpotential was needed for the catholyte-free operation when compared to the standard operation (i.e., electrolyte solution supplied to both cathode and anode) can only be explained by the presence of an electrolyte-like environment. This suggests the crossover of potassium ions (K^+) to the catholyte-free side and water inside the micrometer thin nanomesh electrode. The K^+ is compensated by the OH^- produced via water reduction

reaction therefore creating an *in-operando* electrolyte environment (KOH) on demand, as shown in Fig. 1b. While the focus of state-of-the-art ionomer-free electrodes for AEM water electrolyzers is on the performance metrics of the electrolyzer device, not much is known about the ionic coupling mechanisms in the absence of ionomers.[18–20] In fact, we prove the K^+ ion crossover phenomenon using various physico-chemical characterization techniques and provide new insights in this regard. Moreover, such a phenomenon provided the required ionic coupling between different parts of the Ni nanomesh cathode even in the absence of ionomers, provided that the anode is contacted by a conductive electrolyte. Although the experimental conditions were not targeted towards high-performance AEM water electrolyzer, this paper highlights the mechanism of unintentional transport of cations across an AEM and its potential for ionic coupling, in the absence of added ionomers, hence providing valuable insights for the optimization of AEM electrolyzer systems.

Cation crossover across an AEM is a well-known effect and has been shown to occur in the gas diffusion electrodes of CO_2 electrolyzers with various AEMs including Fumasep, PiperIon and Sustainion causing salt precipitation and variations in the product selectivity.[22–25] This effect comes from the limited permselectivity of commercial AEMs implying that all AEMs display cation crossover and hence aid in establishing ionic coupling via cation crossover, discussed in detail in this work. Therefore, this effect is a universal for all AEMs and not specific to the one used in this work (Fumasep-faa-3–50).

Materials and Methods

Fabrication of Ni nanomesh electrodes.—The step-by-step process flow followed to fabricate the Ni nanomesh electrode is described in our previous reports.[11] In short, a 4 μm thick aluminium layer doped with 0.22 at% Cu prepared by physical vapour deposition on a TiN/Si wafer was fully anodized in 0.3 M oxalic acid (Sigma-Aldrich, ⩾ 99%) by applying 40 V at 30 °C under continuous flow and N_2-bubbling for agitation. This formed the 3D porous anodized aluminium oxide (AAO) template. An etching step of 210 s at ambient temperature in a solution of 1:1:5 volume ratio of ammonia (NH_4OH, CMC Materials 135866), hydrogen peroxide (H_2O_2, 30% Gigabit, KMG 429–136138), and deionized water, respectively, was used to remove any formed TiO_x in the pore bottoms. Following this, sacrificial Cu nanomesh was electroplated within the lower part of the 3D-AAO. Cu electroplating was performed potentiostatically at −0.6 V vs Ag/AgCl until $-0.27\ C\ cm^{-2}_{geo}$ charge density cutoff was reached. Cu plating was performed from a solution containing 5 mM of copper sulphate pentahydrate ($CuSO_4.5H_2O$, Sigma Aldrich 209198) and 20 mM sulfuric acid (H_2SO_4, 96%, Sigma Aldrich, 258105). An inert mixed-metal-oxide (MMO) coated Ti-mesh (Umicore) was used as a counter electrode and the plating solution was maintained at 30 °C. Next, Ni was electroplated at $-5\ mA\ cm^{-2}$ through the 3D-AAO template until it was fully filled with metallic Ni without overplating the template. The plating was performed under constant circulation and agitation through N_2-bubbling at a temperature of 40 °C from a solution containing 350 ml l^{-1} Ni sulfamate ($Ni(SO_3NH_2)_2 \cdot 4H_2O$, 65% w/w concentrate solution, DuPont 12024855), 30 g l^{-1} boric acid (H_3BO_4, Sigma Aldrich, B0394) and 2 ml l^{-1} wetting agent NW (Speciality Electronic Materials). An inert mixed-metal-oxide (MMO) coated Ti-mesh (Umicore) was used as the counter electrode. Next, for the plating of the support structure, we defined the pattern using an open wax mask that was printed on top of the Ni-filled 3D-AAO template. The wax mask was printed using an inkjet printer (PiXDRO LP50). Ni was again plated through the wax mask at $-5\ mA\ cm^{-2}$ for 3600 s to achieve an approximately 4 μm thick support structure. This was then followed by a dissolution of the 3D-AAO and the wax mask in 10% KOH (BASF, 50%) at ambient temperature for 60 min. This finally resulted in the negative structure of the 3D-AAO revealing the nanomesh still attached to the bottom TiN/Si wafer. Next, the sacrificial Cu layer holding the Ni nanomesh to the wafer substrate was etched to obtain free-standing integrated nanomesh electrodes. Cu etching was performed with a freshly prepared 1:1:18 volume ratio of acetic acid (CH_3COOH, glacial, Sigma Aldrich, A6283), hydrogen peroxide (H_2O_2, 30% Gigabit, KMG 429–136138) and de-ionized water, respectively. The nanomesh electrodes detached within 10 min and the floating foil was collected and dried. Finally, the dried nanomesh electrodes were sandwiched between two glass substrates and annealed at 275 °C for 2 h.

Electrolyzer assembly.—Electrolyzer measurements were conducted in a custom-built lab-scale electrolyzer cell. Such a cell was comprised of an outer casing made of two Teflon blocks, each 14 mm thick, which were mechanically supported by stainless-steel plates with a thickness of 3 mm. The inner body of the cell included two Ni flow plates, each 1.5 mm thick, used as current collectors. The Ni flow plates incorporated a parallel channel pattern with 1 mm wide channels for electrolyte circulation and product gas removal. Additionally, 1.5 mm thick silicone gaskets were used to define the exposed electrode area and ensure a leak-proof seal for the electrolyzer.

The size electrodes used measured $3 \times 3\ cm^2_{geo}$, although the area exposed to the electrolyte was limited to $2 \times 2\ cm^2_{geo}$, as defined by the silicone gasket. The nanomesh-membrane-assembly (NMA) was constructed by placing Ni nanomesh electrodes (anode and cathode) on both sides of commercially available AEMs with the nanomesh side facing the membrane.

Effective electrical contact between the Ni flow plates and the NMA was ensured by using 1.5 mm thick commercially available Ni foam (95% porosity, NI00-FA-000152, Goodfellow). The AEMs used in the setup included Fumasep-faa-3–50 and Fumasep-faa-pk-130 with the latter only when Ni foams were used as electrodes. Prior to use, all membranes were soaked in 1 M KOH for a minimum of 24 h to convert them to their OH^- form. Before assembling the electrolyzer cell, all the membranes were thoroughly rinsed with DI water.

Electrolyzer measurements protocol.—Electrochemical measurements on the electrolyzer cell were performed using a Biologic VSP potentiostat equipped with an electrochemical impedance module and connected to a 20 A current booster. Steady-state polarization curves (i-V plots) in 1 M KOH were constructed through galvanostatic experiments across a range of current densities (10–1000 $mA\ cm^{-2}_{geo}$), based on the electrode-exposed footprint area of 4 cm^2_{geo}. Each current density was maintained for 5 min, followed by a galvanostatic electrochemical impedance spectroscopy (GEIS) measurement at the same current density. GEIS measurements were conducted over a frequency range of 100 kHz to 1 Hz, using 8 points per decade and recording 2 measurements per point. The applied current density was superimposed with an alternating current signal having an amplitude equal to 10% of the applied current density. During standard operation, a 1 M KOH electrolyte was supplied at a flow rate of 49 ml min^{-1} to both the anode and cathode. For catholyte-free operation, the flow was directed only to the anode, and for anolyte-free operation, only to the cathode.

DI water flushing experiments were performed in a catholyte-free electrolyzer to verify the crossover of K^+ to the nanomesh cathode. In such an experiment, 10 ml of DI water was circulated through the nanomesh cathode for two minutes to collect any K^+ along with its counterion, most likely OH^- ions. The membranes were not exposed to any KOH prior to the experiment, hence any KOH found must have crossed from the anolyte through the membrane. 10 ml aliquots were taken at OCP after various time periods between 10–40 min and after running the catholyte-free electrolyzer at various current densities, between 200–1000 $mA\ cm^{-2}_{geo}$ with each current density held for 10 min. Subsequently, the conductivity and pH of the collected aliquots were measured, and the samples were submitted for ICP-OES analysis.

Measurement of transport number.—Transport number of a species is defined as the charge carried by that particular species divided by the total charge passed for a given duration of time. In this work, we estimated the transport number for K^+ in the following manner.

DI water flushing experiments, as described above, were performed in a catholyte-free electrolyzer at 400 mA cm^{-2}_{geo} for various times periods to estimate the transport number for K^+. The formula used to estimate the transport number of potassium is described below. First, the concentration of K^+ in the 10 ml aliquots were converted to mols from ppm, based on the measured ICP-OES data. The number of mols of K^+ were then converted to charge and subsequently plotted against the total charge passed during the experiment. The slope of this plot, given as Q_{K^+}/Q_{total}, provides the transport number of K^+.

$$Q_{K^+} = n_{K^+} \times F$$

$$n_{K^+} = \frac{ppm \times V}{1000 \times 39.10}$$

Measurement of contact angles.—The contact angles were measured by sessile drop and captive bubble tests using an OCA 20 optical contact angle measuring and contour analysis system. In the first case, a droplet of deionized water was carefully deposited onto the solid substrate using a dosing needle. The droplet volume was controlled at 3 μl to ensure consistency across all measurements.

In the case of captive bubble tests, the sample was held upside-down and immersed in deionized water. An air bubble with a volume of 3 μl was then introduced beneath the submerged sample surface using a bent dosing needle. The bubble was allowed to stabilize, and its shape was recorded.

The contact angle was determined by analyzing the shape of the droplets and air bubbles, respectively. The measurements were taken at room temperature and repeated at least three times on different spots of the sample to ensure reproducibility. The average contact angle and standard deviation is reported.

Measurement of wicking rate.—The wicking rate was measured by depositing a droplet of deionized water onto the surface of the test sample and recording the process with a high-speed camera. A droplet was placed on the surface using a Legato 111 precision dosing pump and a needle that was placed at approximately 2 mm from the sample surface and dispensed water until the droplet touched the solid surface. An IDT OS4 high-speed camera, set at 1000 frames per second, captured the spread of the droplet over time. All measurements were conducted at room temperature.

The recorded footage was analyzed using custom software to determine the change in the droplet's contact area with the porous surface and the wicking length. The wicking rate was calculated by a linear fit of the wicking length as a function of the square root of time. After a few seconds the evaporation of water from the surface in the open lab environment causes a deviation from the linear fit, which was thus made only using the data of the first 4 s.

Results and Discussion

Electrochemical flow cells such as an electrolyzer (see Fig. 1a) require electrodes that are open on both sides to ensure mass-transport in and out of the porous electrodes. Ni nanomesh electrodes that are open on both sides were obtained by mechanically stabilizing the highly porous nanomesh on an open Ni support structure, together forming an integrated structure as shown in Fig. 1c (more details in Fig. S1). A complete description for the step-by-step process flow and the experimental conditions used for the fabrication of Ni nanomesh electrodes is discussed in our previous work.[11] The nanomesh electrode, with a thickness of just 4 μm, demonstrated significantly better performance compared to commercially available Ni foam electrodes, which are 1600 μm thick, when a 1 M KOH solution was used at both the anode and cathode. In effect, the thinner nanomesh electrodes concentrated all the electrochemical active sites 2-orders of magnitude closer to the membrane whilst maintaining a 110x surface area enhancement. This is the main feature that enables the catholyte-free operation as discussed in the following.

Catholyte-free or anolyte-free electrolyzer operation?.—To evaluate a suitable mode of electrolyzer operation for the Ni nanomesh integrated electrolyzer, steady state i-V data was plotted for standard, catholyte-free and anolyte-free electrolyzer operation as shown in Fig. 2a. Standard electrolyzer operation here means that 1 M KOH electrolyte was supplied to both the anode and cathode compartments. One data point from the steady-state plots, namely 400 mA cm^{-2}_{geo} was chosen to evaluate the electrolyzer performance for longer durations as shown in Fig. 2b. Strikingly, a similar steady-state performance was observed up until 800 mA cm^{-2}_{geo} with or without the presence of an electrolyte supply to the cathode as shown in Fig. 2a (compare curves (1) and (2)). Note that current densities higher than 1 A cm^{-2}_{geo} have been reported in literature, but these are obtained only at higher temperatures of 40 °C–80 °C and using highly active HER/OER catalysts.[26–29] For the lab-scale demonstration in our paper, room temperature was used, for which 1 A cm^{-2} is already at the higher end. Moreover, the catholyte-free operation of this work relies on the wetting of the nanomesh cathode by the transport of water from the anolyte side and through the membrane, as discussed in the following. While water is transported across the membrane to the nanomesh cathode, water is also electrochemically consumed causing a reaction induced drying-up effect. In addition to this, the electro-osmotic drag of water is directed from the cathode to the anode due to the migration of OH^- ions. Therefore, operation up to 1 A cm^{-2}_{geo} was chosen to study crossover without secondary effects. Moreover, interesting approaches to go beyond 1 A cm^{-2}_{geo} and avoid drying-up effects could be to make use of membranes with higher water uptake capacity and kinetics, controlling the gas-liquid pressure across the membrane and by tweaking the nanostructure of the nanomesh electrode to enhance capillary water uptake.

In contrast to the catholyte-free operation, a poorer electrolyzer performance was observed for the anolyte-free operation. In fact, current densities above 600 mA cm^{-2}_{geo} could not be measured in this case. In addition, the galvanostatic current density steps applied (5 min at each current density) to construct the steady state plots of Fig. 2a, show a gradually increasing cell potential at all current densities for the anolyte-free operation as opposed to the stable response obtained for the catholyte-free operation as shown in Fig. 2b (also between 200 and 1000 mA cm^{-2}_{geo} in Fig. S2). This increase in cell voltage for the anolyte-free operation is in fact faster and more evident as the current density is increased.

Figure 2b shows the evolution of cell voltage at galvanostatic 400 mA cm^{-2}_{geo} measured for a longer time (in the hours range). It became clear from this experiment that steady-state conditions were not achievable for the anolyte-free operation. This is seen from the constantly increasing cell voltage from around 2.6 V at a rate of 60 μV s^{-1} to reach the upper cell voltage limit of 2.8 V in less than an hour as shown in the inset of Fig. 2b. The reason behind the failure of anolyte-free operation will become clear with the help of a qualitative model discussed below. Interestingly, in the case of catholyte-free operation, a nearly constant cell voltage of around 2.3 V was recorded for relatively long durations of around 19 h (see curve (4)). This highlights the importance of complementing i-V plots with measurements conducted for longer durations to measure steady state conditions.

To give an idea of reliability and long-term measurement, we operated the nanomesh integrated catholyte-free electrolyzer at 400 mA cm^{-2}_{geo} for 90 h where the anolyte tank was refreshed periodically. Refreshing the anolyte tank was required because of the limited volume, around 125 ml in the small benchtop electrolyzer.

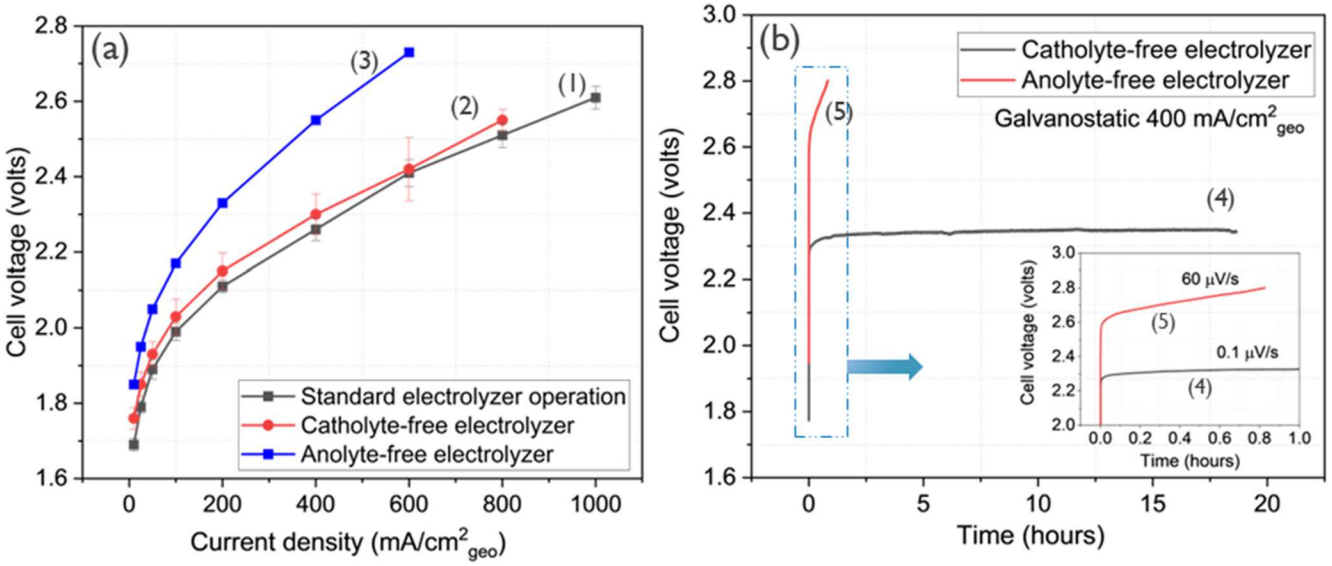

Figure 2. (a) Steady-state polarization curves for Ni nanomesh (4 μm nanomesh + 4 μm support structure) integrated electrolyzer in (1) standard operation, (2) catholyte-free operation and (3) anolyte-free operation. (b) Evolution of cell voltage with time at a fixed current density of 400 mA cm$^{-2}_{geo}$ for Ni nanomesh (4 μm nanomesh + 4 μm support structure) integrated electrolyzer operated in (4) catholyte-free operation and (5) anolyte-free operation. Inset represents the zoom in of the first 1 h of the measurement. The data was recorded at room temperature around 20 °C, atmospheric pressure, with 1 M KOH and with a flow rate of 49 ml min^{-1} and commercial Fumasep FAA-3–50 anion exchange membrane exchanged with OH^-. Error bars represent 90% confidence intervals estimated by repeating the experiment thrice. Standard operation here refers to an electrolyzer operated with 1 M KOH supplied to the anode and cathode at a flow rate of 49 ml min^{-1}.

The cell voltage varied from an initial 2.16 to 2.23 V in the first 45 h after which the anolyte tank was refreshed. Interestingly, the cell voltage recovered to its initial value and quickly reached 2.23 V again for the next 25 h. Similar trend was obtained for the last 20 h of operation post electrolyte renewal (see Fig. S3). This implies that the increase in cell voltage is related to the changing composition of the anolyte and not the loss of intrinsic catalytic activity of the nanomesh electrodes. i.e., loss of water to the cathode and contributions from CO_2 dissolution shifting the pH to lower values. Note that the 90-h long measurements were conducted in a lab scale electrolyzer setup to demonstrate the feasibility of the catholyte-free concept. While operating the catholyte-free electrolyzer for thousands of hours would provide further insights into long-term operation, it is beyond the scope of this work.

Furthermore, we measured the anolyte volume change and pH after the anolyte tank was refreshed during the 90-h long measurement. It was observed that around 35 ml of the anolyte crossed over to the nanomesh cathode in the first 45 h, from which one can estimate a flux of around 5×10^{-8} mol. s^{-1}.cm$^2_{geo}$. Details on the pH and volume changes in the anolyte tank over the 90-h measurement can be found in Table S1. In fact, there is no work studying the electrolyte permeability across an AEM during electrolyzer operation. Generally, the water permeability across AEMs is measured gravimetrically by forcing a water concentration difference across the membrane, and in the absence of external voltage bias.[30] Such measurements would not reflect the actual water fluxes across an AEM during electrolyzer operation. On the other hand, the pH of the anolyte tank did not change significantly during the 90-h measurements.

Finally, postmortem SEM analysis of the nanomesh cathode shows that the nanomesh structure is mostly intact without any significant damage except over the openings of the Ni support structure. It was evident that the nanomesh was blown off over the ~200 microns sized openings of the support structure due to prolonged stress from the gas collection and removal at the openings (see Fig. S4). Moreover, high magnification SEM images show that the nanowires are of similar diameter and the interconnectedness amongst the horizontal and vertical nanowires remain with no evidence of salt precipitation. i.e., carbonate and bicarbonate salt precipitation of K^+ is a well-known problem for CO_2 electrolyzers. In fact, damage caused by the gas collection and removal at the openings of the nanomesh electrode can be significantly minimized by clever designs of the support structure which is on-going work in our lab.

These results demonstrate that the catholyte-free electrolyzer performed as though there was electrolyte present at the cathode ensuring that the active surface area was preserved. This resulted in a similar performance to a standard electrolyzer operation establishing catholyte-free operation as an alternative and viable mode of operation.

Thin nanomesh electrodes are completely wetted.—We suspected that the thinness of the nanomesh electrode (4 μm) allowed it to be completely wet by the water transported across the membrane i.e., wetting of the nanomesh cathode. To visualize the wetting of the nanomesh cathode by the movement of liquid from the anolyte side and through the membrane, we captured videos during catholyte-free operation, from the nanomesh cathode side, at various current densities. For this we used an electrolyzer cell with an open cathode compartment to allow direct imaging with a camera. The electrolyte breakthrough was evident from the videos. In fact, it was observed that the amount of liquid crossing over from the anolyte side increased with increasing current densities (see supplementary material Video S1). Note that, in Video S1, the breakthrough of liquid seems to occur mostly at the edges of the nanomesh cathode. This effect is due to the setup as an O-ring presses the nanomesh cathode to the membrane below minimizing the collection of gas at the nanomesh-membrane interface. In the central region, there is nothing to push the nanomesh to the membrane and hence gas pockets build up pushing all the liquid to the edges. In the actual electrolyzer setup, a Ni foam is placed on the backside of the nanomesh electrode to press it against the membrane and to avoid mechanical damage.

We suspected that the intricate nano structuring of the nanomesh electrode aided the water transport from the anolyte and through the membrane. i.e., the wicking of the nano-capillaries formed in the nanomesh electrode. To illustrate this capillary effect, we measured the evolution of the waterfront inside the nanomesh, after contacting

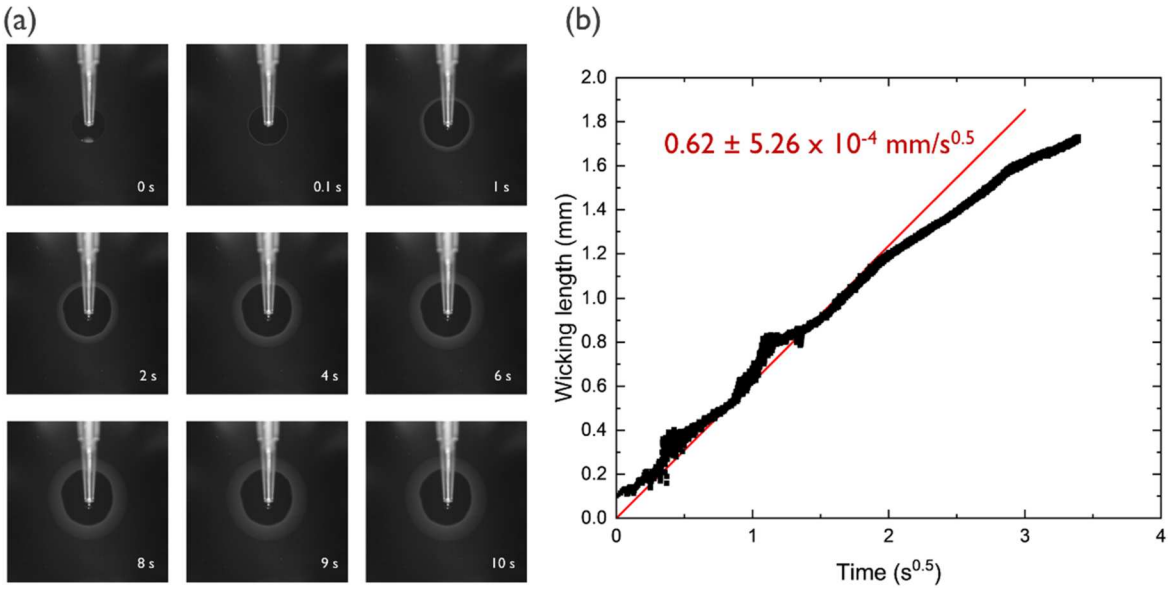

Figure 3. Water wicking experiments conducted on the nanomesh electrode. (a) The rapid time evolution of the waterfront inside the nanomesh electrode captured by a high-speed camera. (b) Scatter plot showing the linear distance travelled by the waterfront as a function of $t^{1/2}$. The linear fit, forced to a zero intercept and acceptable in the lower time periods, gives the wicking rate for the nanomesh electrode. Wicking experiments were performed by dropping a droplet of deionized water on to the surface of the nanomesh electrode. Experiments were performed at ambient conditions.

it with a water droplet, using a high-speed camera (see materials and methods for experimental details). Figure 3a shows the rapid time evolution of the waterfront in the nanomesh electrode. In the time series images shown in Fig. 3a, the tip used to drop the water droplet is seen and the central dark region represents the area which is wetted by the droplet. The width of the bright ring around the central droplet is the wicking length. It is evident that the wicking progresses rapidly in the first 4 s, after which the apparent wicking of the porous structure with water slows down as a result of simultaneous evaporation. In fact, the linear distance travelled by the waterfront plotted as a function of $t^{1/2}$ displayed an initial linear region, for the first 4 s, giving us a wicking rate of around 0.62 mm $s^{-0.5}$.

Additional support to the hydrophilic nature of the nanomesh electrode is provided by water contact angle measurements and captive bubble tests over the nanomesh electrode. Planar Ni substrates were used as reference to draw comparisons with the Ni nanomesh electrode. Water contact angle was measured by placing a droplet of water on the test substrate and evaluating the angle between the droplet and the substrate. On the other hand, a captive bubble test was conducted by immersing the inverted substrate into water and gently placing a gas bubble under the test substrate. This was followed by measuring the angle formed between the gas bubble and the substrate above it. Refer to materials and methods section for experimental details.

Sessile water droplet test and captive bubble test on planar Ni displayed a contact angle of 49 ± 7° and 30 ± 2°, respectively (see Fig. S5 in supplementary). Generally, a water contact angle below 90° indicates that the surface is hydrophilic and that water spreads over the surface. Interestingly, it was impossible to measure the water contact angle on the nanomesh electrodes as the water droplet instantly disappeared spreading into a film (see Video S2). On the other hand, captive bubble tests on the nanomesh electrode showed the opposite behaviour. i.e., gas bubbles did not stick to the nanomesh surface and were off the surface upon detachment from the syringe tip, as seen in Video S2. As such, these results point towards the super hydrophilic wicking nature of the nanomesh electrode which plays a significant role in the water transport from the anolyte, and through the membrane, to the nanomesh cathode.

Next, we tested whether a thin nanostructured cathode is required for catholyte-free operation by comparing the electrolyzer performance of commercially available Ni foam electrodes (1600 μm thick Ni foam used in this work) to our Ni nanomesh electrode. Notice that the Ni foam electrodes are 2 orders of magnitude thicker than the nanomesh electrodes. Steady-state polarization curves for the standard and catholyte-free electrolyzer operation for 1600 μm thick Ni foam electrodes and the same for Ni nanomesh electrodes are shown in Fig. 4. The catholyte-free operation for the 1600 μm thick Ni foam electrodes was dramatically affected when compared to its standard electrolyzer operation (compare curves (4) and (3)). For instance, upon using Ni foam electrodes, the cell potential increased by around 200 mV to 2.55 V at 200 mA cm^{-2}_{geo} for the catholyte-free operation with respect to its standard electrolyzer operation. In fact, current densities above 250 mA cm^{-2}_{geo} could not even be measured in this case. This is mostly attributed to an insufficient wetting of the Ni foam cathode under catholyte-free conditions which decreased the active effective surface area. Moreover, the Ni foam cathode under catholyte-free conditions was observed to be dry after disassembling the electrolyzer (see Fig. S6). On the other hand, the nanomesh electrodes displayed a similar performance with or without a catholyte implying that the nanomesh cathode is completely wet in catholyte-free conditions by the water transported across the membrane. Nyquist plots for the standard and catholyte-free operation and the similar series resistance (R_s) measured at all current densities further support a complete wetting of the nanomesh cathode (see details in Fig. S7). Even after iR-correction, the steady-state voltammograms for standard and catholyte-free operation overlap on one another further indicating a complete wetting of the nanomesh cathode in catholyte-free conditions (see details in Fig. S8). Note that the iR-correction for each operating current density was performed using the R_s measured at the same current density using galvanostatic impedance measurements (see details in Fig. S7 and materials and methods section). It is clear now that the thinness of the nanomesh electrode is what enabled it to be wetted in the absence of a catholyte. However, for an efficient operation of the wetted nanomesh cathode (as observed in this work), it is crucial to have adequate ionic coupling within the nanomesh electrode. Ionic coupling here refers to the ability of different parts of the nanomesh (along the thickness and perpendicular to the membrane) to be in ionic contact.

Concept of catholyte-free electrolyzer operation.—Ionic coupling in traditional CCMs is provided by ionomers which minimizes

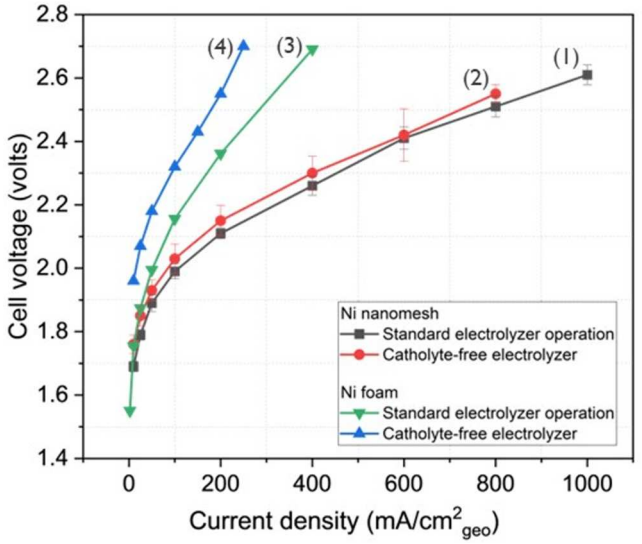

Figure 4. Steady-state polarization curves obtained for Ni nanomesh (4 μm nanomesh + 4 μm support structure) integrated electrolyzer in (1) standard electrolyzer operation, (2) catholyte-free operation and with 1600 μm Ni foam integrated electrolyzer in (3) standard electrolyzer operation, (4) catholyte-free operation. The data was recorded at room temperature around 20 °C, atmospheric pressure, with 1 M KOH and with a flow rate of 49 ml min^{-1} and commercial fumasep-faa-3–50 AEM exchanged with OH^- for Ni nanomesh (4 μm nanomesh + 4 μm support structure) integrated electrolyzer and fumasep-faa-pk-130 for electrolyzer operated with Ni foam. Error bars represent 90 % confidence intervals estimated by repeating the experiment thrice. Standard operation here refers to an electrolyzer operated with 1 M KOH supplied to the anode and cathode at a flow rate of 49 ml min^{-1}.

ohmic potential drop over the electrode and ensures that the entire thickness of the electrode is utilized. Despite not using ionomers in the nanomesh electrodes of this work, a similar steady state i-V response was observed with and without the presence of 1 M KOH as catholyte. The situation is straightforward in the presence of a catholyte, i.e., the potassium hydroxide solution is quite conductive and provides the necessary ionic conductance. As the same performance is achieved for catholyte-free operation, it is clear that ionic coupling is somehow established in the wetted nanomesh cathode of the catholyte-free electrolyzer.

If the nanomesh was only wetted by water from the membrane by crossover from the anolyte, no intrinsic ionic conductivity is present within the porous nanomesh cathode. In this situation only a tiny part of the nanomesh electrode, extremely close to the membrane, will be active. Only within the Donnan region, which extends few nanometers into the water layer, electroreduction of water can operate in electroneutral conditions provided by an electrolyte. Outside this region, the electrode potential drops rapidly and build-up of an additional OH^- charge would result in a voltage penalty (i.e. capacitor). Nevertheless, a similar electrolyzer performance was observed irrespective of the presence of a catholyte implying that the entire nanomesh cathode was utilized under catholyte-free conditions. The only way this can be explained is by considering the crossover of K^+ ions from the anolyte side to the nanomesh cathode via the membrane.

In fact, potassium and cesium ion crossover in an AEM has been visualized using operando X-ray scattering experiments.[23] Interestingly, the K^+ ions were observed to migrate all the way, around 100 μm, to the gas diffusion electrode of a CO_2 electrolyzer operated with 0.1 M $KHCO_3$ as the anolyte and a gas phase CO_2 supply at the cathode. In fact, this unintentional transport of cations across an AEM depends on various factors such as ion exchange capacity (IEC), water uptake, electrochemical potential gradients, operating current density and other physical properties of the membrane.[31] Sufficient water uptake and crossover is especially vital for catholyte-free operation to wet the nanomesh cathode thereby sustaining the applied current density. On the other hand, a high IEC ensures good conductivity for the ion of interest. For example, various research groups have reported the IEC of Fumasep-faa-3–50 (AEM used in this work), in its OH^- form, to be around 1.6–2.2 mmol g^{-1}.[30,32,33] Moreover, the permselectivity of the AEM describing its ability to transport only OH^- is a vital parameter for the successful catholyte-free operation. In this work we make use of the limited permselectivity of commercially available AEMs. In general, the permselectivity of an ion exchange membrane depends on the Donnan exclusion provided by the concentration of fixed ionic groups.[31] When the concentration of co-ions (similar charges in the electrolyte phase as the fixed ionic groups in the membrane) is comparable to the fixed charge density of the membrane, Donnan exclusion is weak and the permselectivity is modest.[24]

To verify the crossover of K^+ to the nanomesh cathode of the catholyte-free electrolyzer, a known amount of DI water was flushed through the nanomesh cathode to collect any K^+ in it, along with its counterion, most likely OH^-. Subsequently, conductivity, pH and ICP-OES measurements were performed on the collected aqueous aliquots (See materials and methods section for experimental details).

Figures 5a and 5b presents the conductivity and pH of the aliquots, respectively, at OCP and after applying various current densities, collected from the flushing experiments. Firstly, it was interesting to observe that the AEMs allowed the movement of KOH across it even without applying a current density, i.e., at OCP. In the duration of 40 min at OCP, the conductivity of the aliquots increased from 0.1 to 0.5 mS cm^{-1} with a corresponding rise in pH from 10.4 to 11.1, respectively, as shown in Fig. 5. This type of K^+-crossover is purely diffusional and originates from the initial concentration gradient. i.e., 1 M KOH at anode and no KOH at cathode. While this process is slow due to the permselectivity of the membrane, we do not see any reason for the diffusion to stop as long as the concentration across the AEM is not balanced out. Note that the reported pH and conductivity values are of the collected aliquots, and not the actual values within the nanomesh cathode where much higher conductivity and pH is expected.

Secondly, the K^+-crossover was significantly enhanced under an applied current density, as indicated by the rapid increase in conductivity and pH shown in Fig. 5. For instance, the conductivity increased from around 0.3 to 3 mS cm^{-1} with a corresponding pH change of around 10.6 to slightly above 12 for current densities between 200 and 1000 mA cm$^{-2}_{geo}$. i.e., an order of magnitude rise in conductivity for slightly more than a unit change in pH which is expected. It is important to realize that the pH of the flushed DI water does not represent the pH inside the nanomesh cathode. There we expect a much higher pH. While the exact reason for the pH to be around 12 for higher current densities is not clear, it can be that the large K^+ concentration built inside the nanomesh resists further buildup of K^+ ions or that the potassium ion collection efficiency is not the same for every flushing experiment. Moreover, it makes sense that the pH stabilizes at higher current densities as an increasing K^+ concentration at the nanomesh cathode will set up a back diffusion of K^+ from the wetted cathode to the anolyte. In fact, pH values in Fig. 5b are only indicative of the KOH formation on the nanomesh cathode side. Furthermore, in this range of current densities, ICP-OES measurements of these aliquots quantified the concentration of K^+ to be between 50–450 ppm. This translates to an equivalent pH between 11–12, assuming a similar OH^- concentration, which matches well with the data presented in Fig. 5b (See SI Fig. S9). Finally, the postmortem XRF analysis of the nanomesh cathode after catholyte-free operation displayed the characteristic potassium-K_α fluorescence peak which was absent for a fresh Ni nanomesh electrode further confirming the crossover of potassium from the anolyte side and through the membrane (See SI Fig. S10).

The process by which ionic coupling is established in the nanomesh electrodes can be understood in three different stages of the catholyte-free electrolyzer operation. Note that, the following explanation to the working mechanism of the catholyte-free concept

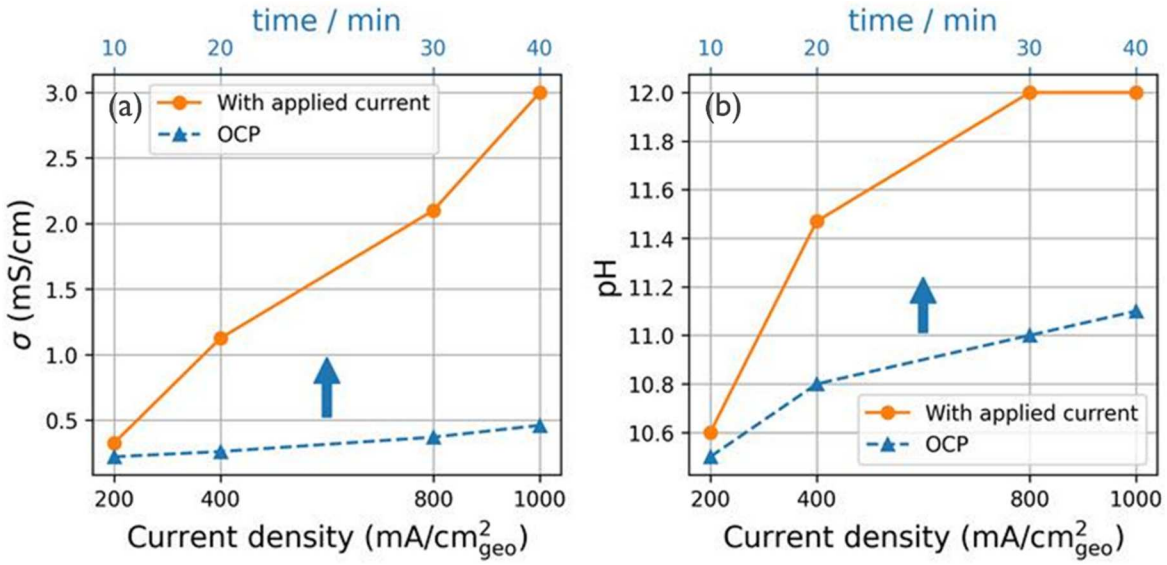

Figure 5. (a) Conductivity and (b) pH of the aqueous aliquots collected by flushing the nanomesh cathode of a catholyte-free electrolyzer with 10 ml of DI water. The DI water flushing experiments were performed for a catholyte-free electrolyzer at OCP as a function of time (10–40 min) and after the application of various current densities (200–1000 mA cm^{-2}_{geo}) for 10 min at each current density. Fresh nanomesh electrodes were used for every current density experiments. Aliquots were collected by circulating 10 ml of DI water through the nanomesh cathode for 2 min to collect any KOH built up during the experiment. Ni nanomesh (4 μm nanomesh + 4 μm support structure) electrodes were used as cathode and anode. The data was recorded at room temperature around 20 °C, atmospheric pressure, with 1 M KOH as the anolyte and with a flow rate of 49 ml min^{-1}. Commercial Fumasep FAA-3–50 anion exchange membrane exchanged with OH^- were used.

only deals with K^+-crossover, and could be an oversimplification to the various processes that are taking place. First, at open circuit conditions, the thin nanomesh cathode is already wetted due to uptake of water from the membrane and fed from the anolyte side. Due to the limited permselectivity of the membrane and the initial concentration gradient, some KOH is dragged along with the water, as shown by the increase in pH and conductivity with time (refer to Fig. 5). Note that, at open circuit conditions, the KOH concentration in the wetted cathode will continuously change with time until equilibrated with the anolyte. However, it is unclear regarding the time scale of such an equilibration process across an AEM.

Secondly, upon applying a current, we observed an anolyte concentration dependent startup phase in the first few minutes, which was quite prominent for the catholyte-free electrolyzer as shown in Fig. 6a. This is characterized by a sharp rise in cell voltage (in the first 5–10 s) which is then followed by a gradual decrease for the next one to two minutes eventually reaching a steady-state plateau. The initial spike in the cell voltage is due to the initially low conductivity in the wetted nanomesh cathode, thereby leading to a high cell voltage. The subsequent rapid drop in the cell voltage is related to an increase in conductivity on the cathode side due to migration of K^+ from the anolyte as depicted in the schematic of Fig. 6b. Moreover, we have already shown that the K^+-crossover is largely dependent on the operating current density (refer to Fig. 5). Note that migration refers to mass transport as result of an electrical field, while diffusion refers to mass transport because of concentration differences. The K^+ ions in the wetted nanomesh cathode, along with an equal fraction of OH^- ions retained due to the charge neutrality rule (i.e., the sum of OH^- and K^+ transport numbers is 1), and formed by the water reduction reaction, led to the formation of KOH on demand. In fact, the concentration of K^+ increases until it is balanced by a diffusive flux in the opposite direction (from cathode to anode) after which there is zero net flux of K^+, describing steady-state conditions as shown in Fig. 6b. Note that the majority of the ion transport over the membrane is carried by OH^- ions with only a minimal contribution by K^+. In fact, the transport number was estimated to be around 0.004, implying only 0.4% of the total charge was carried by the potassium ions. This was evaluated from the slope of the plot between the charge carried by K^+ as a function of the total charge passed (See SI Fig. S11 for more details). Note, the methodology used to estimate the transport number is detailed in the materials and methods section. While such low transport numbers for cations across an AEM is logical, it is important to realize that even such minimal contributions can introduce sufficient ionic coupling when the electrodes are thin enough, such as our nanomesh. On the other hand, it makes sense that the minimal crossover of K^+ can already provide sufficient ionic coupling, as the nanomesh electrode is only a few microns thick with a porosity of around 75%. i.e., the nanomesh electrode can only hold around 0.3 μl cm^{-2}_{geo} of water in its empty volume.

Thirdly, following the startup phase, steady state conditions were achieved in catholyte-free conditions comparable to the standard electrolyzer operation. The in situ formed KOH provided the ionic coupling in the nanomesh cathode and at steady-state, the concentration of KOH at the wetted nanomesh cathode is expected to be larger than the anolyte concentration (1 M KOH) as shown in Fig. 6c. This larger KOH concentration in the wetted nanomesh cathode is required for the diffusive K^+ flux from the wetted nanomesh cathode counteracting its migration from the anolyte, hence leading to steady-state conditions (see Fig. 6b). Additionally, the initial startup phase was observed every time the catholyte-free electrolyzer was brought out of sufficient rest from open circuit conditions, by supplying a fixed current density (prominent at current densities above 200 mA cm^{-2}_{geo}). This suggests that the K^+ crossover is reversible and that a new steady-state concentration needs to be re-established, further supporting our hypothesis that the KOH concentration in the wetted nanomesh cathode is larger than the 1 M KOH in the supplied anolyte. Considering the use of relatively high concentrations of KOH (1 M or more) and the thinness of the nanomesh electrode (4 microns), we do not expect to have internal variations in the concentration of KOH within the nanomesh electrode. Local variations in KOH concentration within the nanomesh is suspected during the start-up phase of the catholyte-free electrolyzer where the interplay between migration and diffusion of K^+ and OH^- species quickly establishes steady-state conditions. Although advanced characterizations measuring in situ and inside the few micrometers thin nanomesh would bring further insights, such characterization is far from straight forward for few microns

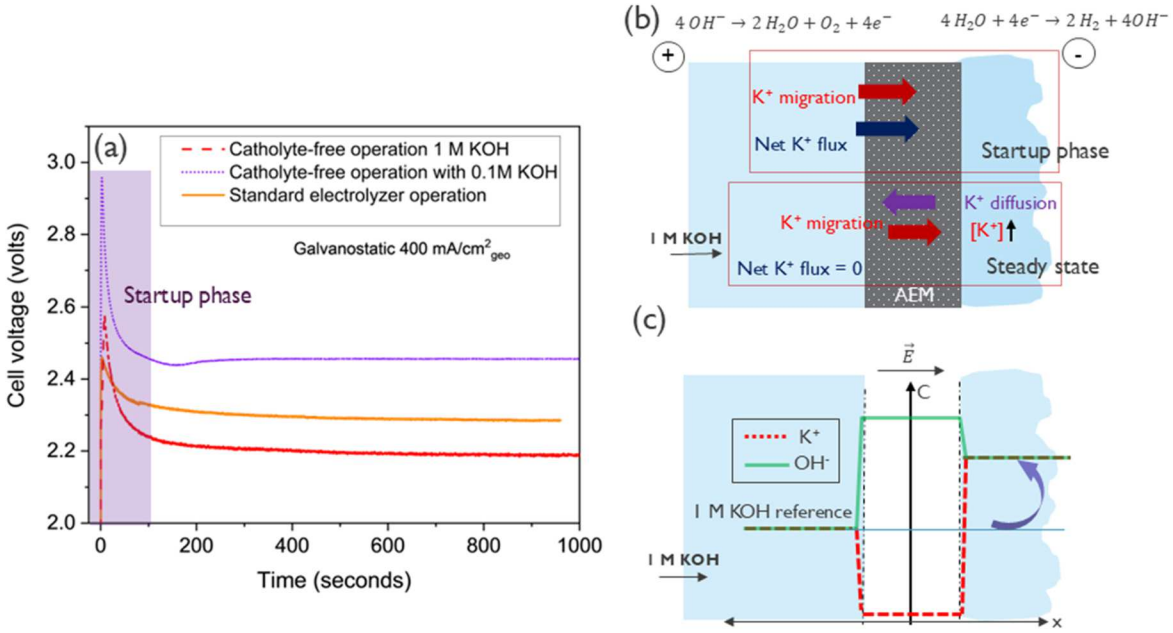

Figure 6. (a) Evolution of cell voltage with time at a fixed current density of 400 mA cm^{-2}_{geo} for a Ni nanomesh (4 μm nanomesh + 4 μm support structure) integrated electrolyzer operated in catholyte-free mode (with 1 M KOH and 0.1 M KOH anolyte supply) and standard operation. Schematic diagrams for the operation of a catholyte-free electrolyzer displaying (b) the migration and diffusion flux of K^+ at startup phase and at steady state conditions, (c) The expected steady state concentration profiles of K^+ and OH^-. Standard operation here refers to an electrolyzer operated with 1 M KOH supplied to the anode and cathode at a flow rate of 49 ml min^{-1}.

nanomaterial, and would need specific developments that is beyond the scope of this work. Instead, we have chosen to expand and elaborate on the quantitative analysis already provided with ex situ ICP-OES, XRF measurements, pH and conductivity measurements, combined with a logical qualitative model as discussed above.

Now, the reason behind the poor performance of the anolyte-free electrolyzer becomes clear also. Initially, the wetted nanomesh anode of the anolyte-free electrolyzer must have had some KOH in it most likely from the crossover due to diffusion at OCP. Otherwise, we would have observed a cell voltage overload instantly after applying a fixed current density, which is not the case. In fact, the anolyte-free electrolyzer seemed to operate quite well at current densities between 10–600 mA cm^{-2}_{geo} for the first 10 min (see SI Fig. S2). It was only at the end of around 1 h, at 400 mA cm^{-2}_{geo}, that we observed that the anolyte-free electrolyzer failed (as shown in Fig. 2b). From the initial KOH present at the wetted nanomesh anode, electromigration now drives K^+ away from the nanomesh which simultaneously consumes the OH^- to form oxygen gas. Although OH^- is the major charge carrier, the tiny charge carried away by the K^+ from the wetted anode due to electromigration invariably leads to a time dependent and constant depletion of KOH from the wetted nanomesh anode (see SI Fig. S12a). This lowers the ionic conductivity in the wetted anode with time and is indeed observed as a time dependent increase in cell voltage to eventually reach a cell voltage cutoff as that of Fig. 2b. Such an argument is further supported by the fact that we observed the time dependent cell voltage increase to be more drastic as the operating current density was increased (details in Fig. S2). Moreover, the K^+ cannot be replenished in the absence of an anolyte supply. Although at steady-state conditions, one can expect a diffusive flux from the catholyte to counteract the migration of K^+ from the wetted anode, the concentration of KOH can be extremely low or can even go to zero (see SI Fig. S12b) hence breaking the ionic coupling within the porous wetted nanomesh anode.

Thicker AEMs would most likely lead to higher initial cell voltage spikes in the start-up phase due to a larger iR-drop. However, in steady-state conditions, the catholyte-free electrolyzer is expected to operate similar to its standard electrolyzer operation for all AEMs. While we did not study the catholyte-free operation and K^+-crossover with various thickness/types of commercial AEMs, this work reports the concept of K^+ crossover across one particular AEM, Fumasep-FAA-3–50, and how it can facilitate ionic coupling in catholyte-free electrolyzers operating with ionomer-free electrodes.

Finally, while the catholyte-free operation discussed in this work offers an easier mode of lab-scale operation, scaling this up to the system level might pose various challenges. This includes removal of entrained electrolytes in the hydrogen output, managing hydrostatic pressure across the membrane for larger electrode assemblies and thermal management, especially at the cathodes. Generally, the liquid electrolyte flow on both sides of a stack apart from reagent and product transport also help cool the system due to the high heat capacity of water. For an electrolyzer stack operating in catholyte-free mode, heat must go through the membrane and then be cooled by the circulating liquid anolyte. Since the membrane is quite thin, this way of heat removal may be viable but requires testing. On the other hand, while the membrane and the circulating anolyte could help in heat removal from the cathodes, it may not be sufficient. Moreover, higher temperatures, especially over the cathode, can result in increased evaporation of the water layers leading to water mass transport limitations. However, tolerable rise in temperature can enhance kinetics simply by heating as described by the Arhenius law. In fact, commercial PEM electrolyzers also operate without catholyte supply where secondary cooling systems are often used. Here, secondary cooling systems refer to external cooling towers and heat exchangers required to efficiently cool the exiting DI water. Furthermore, we suspect that the K^+-crossover to also be affected by temperature, although not studied in this work. Generally, diffusional flux (due concentration gradient) is a strongly dependent on temperature implying that the diffusion component of the cation crossover must increase with rise in temperature. This is mostly due to the reduced viscosity of the electrolyte medium thereby enhancing the diffusion coefficient of the species. On the other hand, the flux due to electromigration (due to electric field) is more or less temperature independent due to the weak dependence between mobility and temperature. While this work establishes that the K^+-crossover during catholyte-free operation is mostly due to electromigration, increasing temperature can cause significant change in the diffusional flux therefore enhancing the overall cation crossover.

Conclusions

In this work, we propose an alternate and easier means of operating our Ni nanomesh integrated AEM water electrolyzer by going catholyte-free. The thin form factor of the nanomesh electrodes combined with the intrinsic property of membranes to allow tiny amounts of water to pass through enabled this catholyte-free operation. First, it was shown that the few microns thin nanomesh electrodes were completely wetted, ensuring that the active surface area was preserved. Secondly, the required ionic coupling in the porous wetted nanomesh cathode was provided by operando KOH electrolyte environment thereby eliminating the need for any ionomers. Such a process occurred due to the migration driven K^+ flux (from the anolyte to the wetted nanomesh cathode across the AEM) which retained some of the OH^- produced via water reduction reaction in the initial startup phase, hence forming KOH on demand, locally within the wetted nanomesh cathode. The intention of this work is not to present a high-performance AEM water electrolyzer but to highlight the fact that unintentional cation transport across an AEM can be used to our benefit. Since this way of establishing ionic coupling relies on the tiny charge carried by the counter-ions (K^+ in this work), we predict that PEM electrolyzers could operate in anolyte-free conditions where the sulphate (SO_4^{2-}) and the bisulphate (HSO_4^-) ions would behave analogous to the potassium ions of this work.

In our understanding, such an operando KOH formation is not only limited to our nanomesh electrodes but can possibly occur even in traditional CCMs of AEM water electrolyzers operating with low concentration potassium hydroxide solution at the anode. This alternate way of establishing ionic coupling can lead to a better understanding of our dependence on ionomers. Furthermore, significant improvements on the performance of the catholyte-free electrolyzer is possible by controlling the extent of flooding hence making it easier for the produced H_2 to escape, tuning the support structure geometry to facilitate gas removal, selecting the right experimental conditions such as temperature to minimize the equilibrium potential, and using highly active HER catalysts for enhanced kinetics. In fact, a well-controlled wetting can enable efficient electrochemical reduction reactions of reactants that are sparingly soluble in water such as CO_2 and N_2. For instance, a thinner wetting layer ensures that the CO_2 molecules diffuse faster in the gas phase compared to its slow diffusion and low solubility in the liquid phase. Controlling this directly affects the achievable limiting currents for CO_2 electroreduction. Moreover, since the operando-KOH is only localized in the nanomesh cathode, CO_2 losses to carbonates and bicarbonates can also be restricted within the nanomesh region and hence minimized, a topic which will be the subject of future work. Finally, when considering an electrolyzer stack (series of electrolytic cells), the conductive electrolytes supplied via manifolds also behave as bypass pathways for ionic shunt currents and reverse currents. The catholyte-free electrolyzer reported in this work is interesting for remedying such undesired current losses as it eliminates the medium via which shunting of ionic current takes place.

Acknowledgments

The authors would like to thank Allyssa Massie, Researcher at imec for her feedback on the manuscript. We would also like to extend our gratitude to the MCA group at imec for sample preparation and SEM analysis. We also thank Eros Billen, facilities assistant at imec, for performing ICP-OES measurements for us. Finally, we extend our gratitude to Debargha Chakravorty, PhD student at KU-Leuven and imec, and Sukhvinder Singh, Researcher at imec for their assistance in XRF related experiments.

Data Availability Statement

The authors confirm that the data supporting the findings of this study are available within the article and/or its supporting information. Additional data if required is available on request from the authors.

ORCID

Venkataramana Rishikesan https://orcid.org/0000-0002-9975-742X
Martijn J. W. Blom https://orcid.org/0000-0002-4350-7085
Patrick Steegstra https://orcid.org/0000-0002-0871-808X
Rico Rupp https://orcid.org/0000-0003-0684-2658
Philippe M. Vereecken https://orcid.org/0000-0003-4115-0075

References

1. C. Li and J. B. Baek, "The promise of hydrogen production from alkaline anion exchange membrane electrolyzers." *Nano Energy*, **87**, 106162 (2021).
2. I. Vincent and D. Bessarabov, "Low cost hydrogen production by anion exchange membrane electrolysis: a review." *Renew. Sustain. Energy Rev.*, **81**, 1690 (2018).
3. S. Marini, P. Salvi, P. Nelli, R. Pesenti, M. Villa, M. Berrettoni, G. Zangari, and Y. Kiros, "Advanced alkaline water electrolysis." *Electrochim. Acta*, **82**, 384 (2012).
4. I. Vincent, A. Kruger, and D. Bessarabov, "Development of efficient membrane electrode assembly for low cost hydrogen production by anion exchange membrane electrolysis." *Int. J. Hydrogen Energy*, **42**, 10752 (2017).
5. S. A. Lee, J. Kim, K. C. Kwon, S. H. Park, and H. W. Jang, "Anion exchange membrane water electrolysis for sustainable large-scale hydrogen production." *Carbon Neutralization*, **1**, 26 (2022).
6. Q. Li et al., "Anion exchange membrane water electrolysis: the future of green hydrogen." *J. Phys. Chem. C*, **127**, 7901 (2023).
7. M. Moreno-González, P. Mardle, S. Zhu, B. Gholamkhass, S. Jones, N. Chen, B. Britton, and S. Holdcroft, "One year operation of an anion exchange membrane water electrolyzer utilizing Aemion+® membrane: minimal degradation, low H2 crossover and high efficiency." *Journal of Power Sources Advances*, **19**, 100109 (2023).
8. P. Fortin, T. Khoza, X. Cao, S. Y. Martinsen, A. Oyarce Barnett, and S. Holdcroft, "High-performance alkaline water electrolysis using AemionTM anion exchange membranes." *J. Power Sources*, **451**, 227814 (2020).
9. S. P. Zankowski and P. M. Vereecken, "Electrochemical determination of porosity and surface area of thin films of interconnected nickel nanowires." *J. Electrochem. Soc.*, **166**, D227 (2019).
10. S. P. Zankowski and P. M. Vereecken, "Combining high porosity with high surface area in flexible interconnected nanowire meshes for hydrogen generation and beyond." *ACS Appl. Mater. Interfaces*, **10**, 44634 (2018).
11. N. Plankensteiner, R. Rupp, P. Steegstra, S. Singh, J. G. Canto, S. Wodarz, M. J. W. Blom, J. John, M. Mees, and P. M. Vereecken, "Freestanding μm-thin nanomesh electrodes exceeding 100x current density enhancement for high-throughput electrochemical applications." *Materials Today Energy*, **30**, 101172 (2022).
12. N. Guruprasad, J. van der Schaaf, and M. T. de Groot, "Unraveling the impact of reverse currents on electrode stability in anion exchange membrane water electrolysis." *J. Power Sources*, **613**, 234877 (2024).
13. M. Z. Yang, H. Wu, and J. R. Selman, "A model for bipolar current leakage in cell stacks with separate electrolyte loops." *J. Appl. Electrochem.*, **19**, 247 (1989).
14. A. T. Kuhn and J. S. Booth, "Electrical leakage currents in bipolar cell stacks." *J. Appl. Electrochem.*, **10**, 233 (1980).
15. G. Sakas, A. Ibáñez-Rioja, V. Ruuskanen, A. Kosonen, J. Ahola, and O. Bergmann, "Dynamic energy and mass balance model for an industrial alkaline water electrolyzer plant process." *Int. J. Hydrogen Energy*, **47**, 4328 (2022).
16. S. Favero, I. E. L. Stephens, and M. M. Titirci, "Anion exchange ionomers: design considerations and recent advances - an electrochemical perspective." *Adv. Mater.*, **36**, 2308238 (2024).
17. S. Koch, P. A. Heizmann, S. K. Kilian, B. Britton, S. Holdcroft, M. Breitwieser, and S. Vierrath, "The effect of ionomer content in catalyst layers in anion-exchange membrane water electrolyzers prepared with reinforced membranes (Aemion +TM)." *J. Mater. Chem. A*, **9**, 15744 (2021).
18. T. H. Kong, P. Thangavel, S. Shin, S. Kwon, H. Choi, H. Lee, N. Park, J. J. Woo, and Y. Kwon, "In-situ ionomer-free catalyst-coated membranes for anion exchange membrane water electrolyzers." *ACS Energy Lett.*, **8**, 4666 (2023).
19. E. López-Fernández, C. Gómez-Sacedón, J. Gil-Rostra, J. P. Espinós, A. R. González-Elipe, F. Yubero, and A. de Lucas-Consuegra, "Ionomer-free nickel-iron bimetallic electrodes for efficient anion exchange membrane water electrolysis." *Chem. Eng. J.*, **433**, 133774 (2022).
20. E. López-Fernández, C. Gómez-Sacedón, J. Gil-Rostra, J. P. Espinós, J. J. Brey, A. R. González-Elipe, A. de Lucas-Consuegra, and F. Yubero, "Optimization of anion exchange membrane water electrolyzers using ionomer-free electrodes." *Renewable Energy*, **197**, 1183 (2022).
21. V. Rishikesan, M. J. W. Blom, and P. M. Vereecken, "Ionomer-free electrolysis of DI water enabled by confined in situ electrolyte generation in Pt nanomesh electrodes." *Chem. Eng. J.*, **508**, 160758 (2025).
22. Á. Vass, B. Endrődi, G. F. Samu, Á. Balog, A. Kormányos, S. Cherevko, and C. Janáky, "Local chemical environment governs anode processes in CO2Electrolyzers." *ACS Energy Lett.*, **6**, 3801 (2021).
23. A. B. Moss, S. Garg, M. Mirolo, C. A. Giron Rodriguez, R. Ilvonen, I. Chorkendorff, J. Drnec, and B. Seger, "In operando investigations of oscillatory water and carbonate effects in MEA-based CO2 electrolysis devices." *Joule*, **7**, 350 (2023).
24. G. A. El-Nagar, F. Haun, S. Gupta, S. Stojkovikj, and M. T. Mayer, "Unintended cation crossover influences CO2 reduction selectivity in Cu-based zero-gap electrolysers." *Nat. Commun.*, **14**, 2062 (2023).

25. A. Kiessling et al., "Influence of supporting electrolyte on hydroxide exchange membrane water electrolysis performance: anolyte." *J. Electrochem. Soc.*, **168**, 084512 (2021).
26. A. W. Tricker, J. K. Lee, J. R. Shin, N. Danilovic, A. Z. Weber, and X. Peng, "Design and operating principles for high-performing anion exchange membrane water electrolyzers." *J. Power Sources*, **567**, 232967 (2023).
27. J. E. Park, S. Y. Kang, S. H. Oh, J. K. Kim, M. S. Lim, C. Y. Ahn, Y. H. Cho, and Y. E. Sung, "High-performance anion-exchange membrane water electrolysis." *Electrochim. Acta*, **295**, 99 (2019).
28. Y. Zheng, W. Ma, A. Serban, A. Allushi, and X. Hu, "Anion Exchange Membrane Water Electrolysis at 10 A $\cdot$ cm^{-2} Over 800 h." *Angewandte Chemie - International Edition*, **64**, e202413698 (2025), Anion Exchange Membrane Water Electrolysis at 10 A $\cdot$ cm^{-2} Over 800 h.
29. L. Li et al., "Production of the porous transport layer based on stainless steel felt for anion exchange membrane water electrolysis." *Electrochim. Acta*, **513**, 145598 (2025).
30. H. Khalid, M. Najibah, H. S. Park, C. Bae, and D. Henkensmeier, "Properties of anion exchange membranes with a focus on water electrolysis." *Membranes*, **12**, 989 (2022).
31. P. Aydogan Gokturk, R. Sujanani, J. Qian, Y. Wang, L. E. Katz, B. D. Freeman, and E. J. Crumlin, "The Donnan potential revealed." *Nat. Commun.*, **13**, 5880 (2022).
32. M. Roschger, S. Wolf, A. Billiani, K. Mayer, M. Hren, S. Gorgieva, B. Genorio, and V. Hacker, "Study on commercially available membranes for alkaline direct ethanol fuel cells." *ACS Omega*, **8**, 20845 (2023).
33. X. Luo, S. Rojas-Carbonell, Y. Yan, and A. Kusoglu, "Structure-transport relationships of poly(aryl piperidinium) anion-exchange membranes: eeffect of anions and hydration." *J. Membr. Sci.*, **598**, 117680 (2020).